III-Nitride nanophotonics for beyond-octave soliton generation and self-referencing

Xianwen Liu
Yale University https://orcid.org/0000-0001-7398-4387
Zheng Gong
Yale University
Alexander Bruch
Yale University https://orcid.org/0000-0002-3666-8606
Joshua Surya
Yale University
Juanjuan Lu
Yale University
Hong Tang (hong.tang@yale.edu)
Yale University https://orcid.org/0000-0001-5374-2137

Article

Keywords: nanophotonics, optics

Posted Date: February 8th, 2021

DOI: https://doi.org/10.21203/rs.3.rs-134626/v1

Version of Record: A version of this preprint was published at Nature Communications on September 14th, 2021. See the published version at https://doi.org/10.1038/s41467-021-25751-9.

III-Nitride nanophotonics for beyond-octave soliton generation and self-referencing

Xianwen Liu,[1] Zheng Gong,[1] Alexander W. Bruch,[1] Joshua B. Surya,[1] Juanjuan Lu,[1] and Hong X. Tang[1,2]

[1] *Department of Electrical Engineering, Yale University, New Haven, CT 06511, USA*

[2] *Corresponding author: hong.tang@yale.edu*

(Dated: December 23, 2020)

Frequency microcombs, successors to mode-locked laser and fiber combs, enable miniature rulers of light for applications including precision metrology, molecular fingerprinting and exoplanet discoveries. To enable frequency ruling functions, microcombs must be stabilized by locking their carrier-envelop offset frequency. So far, the microcomb stabilization remains compounded by the elaborate optics external to the chip, thus evading its scaling benefit. To address this challenge, here we demonstrate a nanophotonic chip solution based on aluminum nitride thin films, which simultaneously offer optical Kerr nonlinearity for generating octave soliton combs and Pockels nonlinearity for enabling heterodyne detection of the offset frequency. The agile dispersion control of crystalline III-Nitride photonics permits high-fidelity generation of solitons with features including 1.5-octave spectral span, dual dispersive waves and sub-terahertz repetition rates down to 220 gigahertz. These attractive characteristics, aided by on-chip phase-matched aluminum nitride waveguides, allow the full determination of the offset frequency. Our proof-of-principle demonstration represents an important milestone towards fully-integrated self-locked microcombs for portable optical atomic clocks and frequency synthesizers.

I. INTRODUCTION

Optical frequency combs, originally developed from solid-state or fiber based mode-locked lasers, have evolved into photonic-chip-based sources that are compact, robust and power efficient [1]. Among various chipscale schemes [2–5], microresonator Kerr frequency combs ("microcombs" hereafter) are of particular interest because of their high scalability for photonic integration [6–8]. Indeed, substantial efforts have been made towards soliton mode-locking, allowing phase coherent microcombs on the one hand [9–17] and unveiling rich soliton physics on the other hand [18–20]. Specifically, octave-spanning soliton microcombs permit phase locking of the carrier-envelop offset (CEO) frequency (f_{ceo}) via well-known f–$2f$ interferometry [21], and are prerequisite for chip-scale implementation of precision metrology [22], frequency synthesizers [23] and optical clocks [24]. To date, silicon nitride (Si_3N_4) nanophotonics has proved viable for octave soliton operations with a terahertz repetition rate (f_{rep}) [25–27]. Nevertheless, such a large f_{rep} is not amenable for direct photodetection and poses challenges to access the CEO frequency with a value up to f_{rep}. In the meantime, the lack of intrinsic quadratic $\chi^{(2)}$ nonlinearities in Si_3N_4 films typically requires an external frequency doubler and off-chip optical circuitry for deriving the CEO frequency [28, 29]. These off-chip optical components compromise the scaling advantage of microcombs and significantly set back self-locked microcombs for portable applications.

III-Nitride semiconductors such as aluminum nitride (AlN) exhibit a non-centrosymmetric crystal structure, thereby possessing inherent optical $\chi^{(2)}$ nonlinearity as well as Pockels electro-optic and piezoelectric properties [30]. Apart from the advances in ultraviolet light-emitting diodes [31] and quantum emitters [32, 33], AlN has also proved viable for low-loss nanophotonics in high-efficiency second-harmonic generation (SHG) [34, 35] and high-fidelity Kerr and Pockels soliton mode-locking [15, 36]. Therefore, it is feasible to establish an on-chip f–$2f$ interferometer provided that an octave AlN soliton microcomb is available. This is a solution that is favored here comparing with the heterogeneous integration approach such as proposal based on hybrid gallium arsenide (GaAs)/Si_3N_4 waveguides [37]. Despite that on-chip f_{ceo} detection was achieved from supercontinuua driven by a femtosecond laser in non-resonant $\chi^{(2)}$ nanophotonic waveguides made from AlN [38] or lithium niobate (LN) thin films [39, 40], resonator microcomb-based f–$2f$ interferometry using nanophotonics, to our knowledge, remains elusive.

In this article, we demonstrate high-fidelity generation of octave soliton microcombs and subsequent f_{ceo} detection using AlN-based nanophotoinc chips. Thanks to mature epitaxial growth, AlN thin films with highly uniform thickness are available, thus permiting lithographic control of group velocity dispersion (GVD) for comb spectral extension via dispersive wave (DW) emissions [11]. Our octave soliton microcombs possess separated dual DWs and moderate f_{rep} of 433, 360 and 220 gigahertz, and are found to be reproducible from batch-to-batch fabrications. The results then allow us to capture the f–$2f$ beatnote through on-chip SHG in phase-matched AlN waveguides. Our work establish the great potential of non-centrosymmetric III-Nitride photonic platforms for portable self-locked microcomb sources.

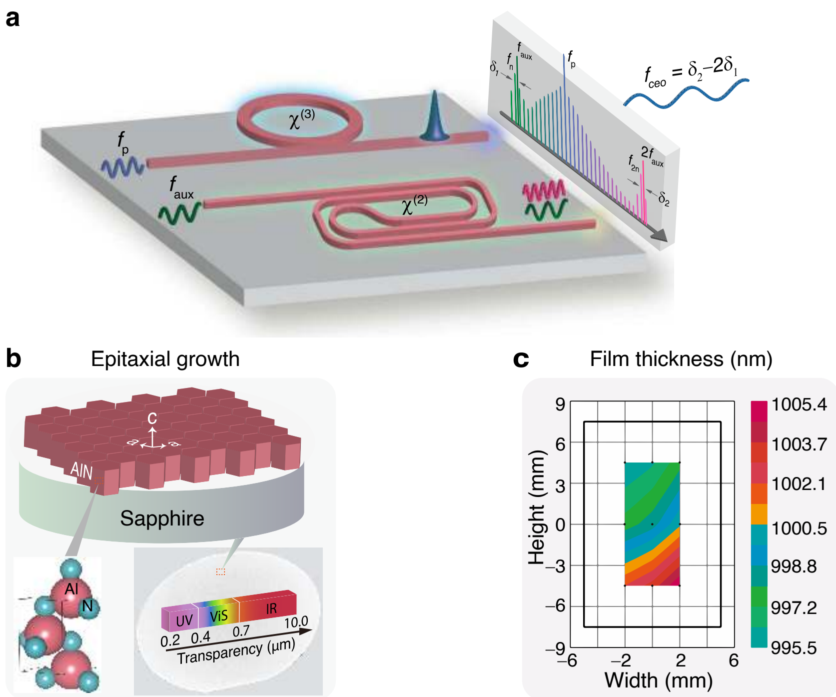

Fig. 1. **Experimental scheme**. **a**. Illustration of f–$2f$ interferometry using octave-spanning soliton microcombs and second-harmonic generators in a nanophotonic platform harboring simultaneous $\chi^{(3)}$ and $\chi^{(2)}$ susceptibilities. The offset frequency $f_{\rm ceo}$ is accessible from the beatnotes of δ_1 and δ_2, and $f_{\rm p}$ is the pump laser frequency. **b**. Top: sketch of a hexagonal AlN layer (lattice constants: a and c) epitaxially grown on a c-plane sapphire substrate. Bottom: unit cell of an AlN crystal (left) and photograph image of a 2-inch AlN wafer featuring a broad transparency window from ultraviolet to mid-infrared regimes (right). **c**. Spectroscopic ellisometer mapping of the AlN film thickness in a region of $4\times 9\,\mathrm{mm}^2$, showing a minor variation of $1000\pm 5\,\mathrm{nm}$ denoted by the right color bar.

II. RESULTS

Experimental scheme description. Figure 1a illustrates the implementation of microcomb-based f–$2f$ interferometry using nanophotonic chips. The strategy is to leverage non-centrosymmetric photonic media for simultaneous integration of $\chi^{(3)}$ octave soliton microcombs and $\chi^{(2)}$ SHG doublers. For a proof-of-principle demonstration, we adopt an auxiliary laser (at $f_{\rm aux}$) to obtain sufficient SHG power (at $2f_{\rm aux}$) from phase-matched optical waveguides. The use of the auxiliary laser can be eliminated by exploiting microring-based architecture to boost the SHG efficiency [34]. By subsequently beating $f_{\rm aux}$ and $2f_{\rm aux}$ with the $f_{\rm n}$ and $f_{\rm 2n}$ comb lines at their corresponding beatnotes of δ_1 and δ_2, the $f_{\rm ceo}$ signal reads:

$$f_{\rm ceo} = \delta_2 - 2\delta_1 \tag{1}$$

The AlN thin films in this work were epitaxially grown on a c-plane sapphire substrate via metal-organic chemical vapour deposition [41, 42]. As illustrated in Fig. 1b, the AlN crystals exhibit a hexagonal wurtzite structure with a unit cell shown in the bottom, highlighting the non-centrosymmetry. We also show an overall 2-inch AlN-on-sapphire wafer featuring a broadband transparency and a favored film thickness (Fig. 1c)–both are crucial factors to ensure octave GVD control. Great attention was also paid to the film crystal quality and surface roughness for low-loss photonic applications. The AlN nanophotonic chips were manufactured following electron-beam lithography, chlorine-based dry etching and silicon dioxide (SiO_2) coating processes and were subsequently cleaved to expose waveguide facets [43]. The intrinsic optical quality factors ($Q_{\rm int}$) of the AlN resonators were characterized to be ~1–3 million depending on the waveguide geometries. The detailed film and device characterization is presented in Methods and Supplementary Section I.

Since wurtzite AlN manifests optical anisotropy for vertically or horizontally-polarized light [44], we engineer the waveguide structures for optimal operation of fundamental transverse magnetic (TM_{00}) modes, which allows the harness of its largest $\chi^{(2)}$ susceptibility to ensure high-efficiency SHG. To expand microcomb spectra out of the anomalous GVD restriction, we exploit soliton-induced DW radiation by tailoring the resonator's integrated dispersion ($D_{\rm int}$) [11]:

$$D_{\rm int} = \frac{D_2}{2!}\mu^2 + \frac{D_3}{3!}\mu^3 + \sum_{i\geq 4}\frac{D_i}{i!}\mu^i \tag{2}$$

where D_2, D_3, and D_i are $i_{\rm th}$-order GVD parameters,

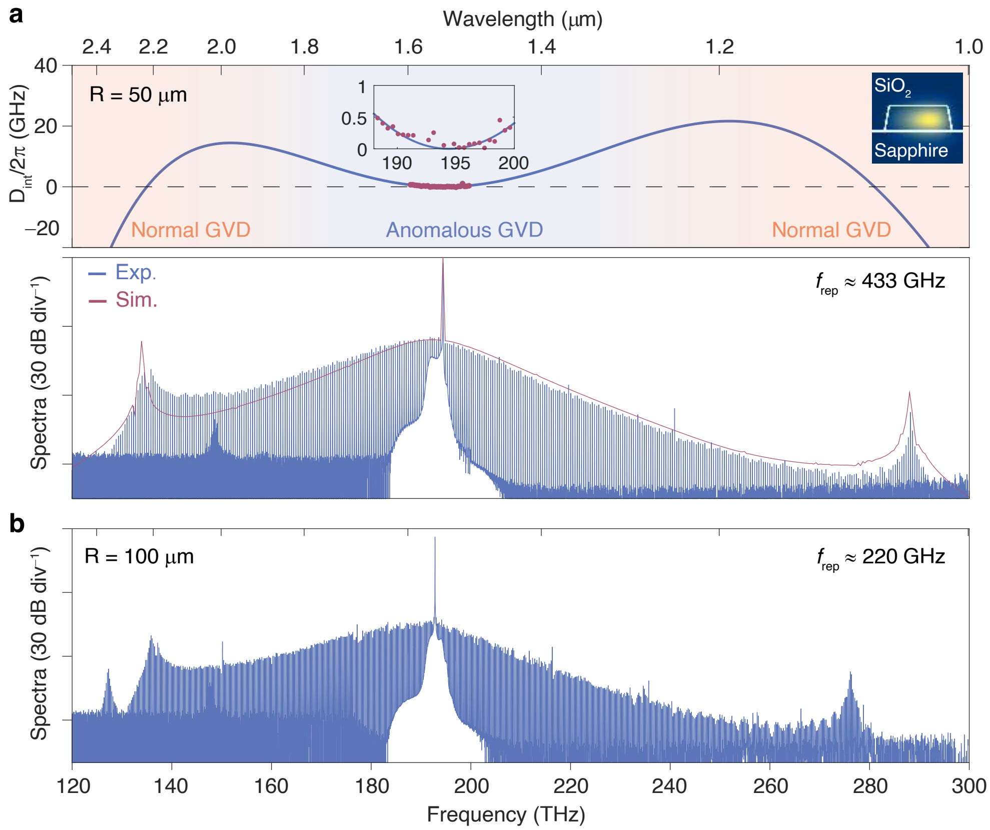

Fig. 2. **Octave soliton microcombs at hundreds of gigahertz repetition rates**. **a**. Top: integrated dispersion (D_{int}) of a $50\,\mu$m-radius AlN resonator (cross section: $1.0\times2.3\,\mu\mathrm{m}^2$), where the anomalous and normal GVD regimes are shaded with light blue and orange colors respectively. Insets: zoom-in view of the measured (red dots) and simulated (blue curve) values and the resonator modal profile shown in the right. Bottom: soliton microcomb spectra from the experiment (blue) and simulation (red) at an on-chip pump power of $\sim$390 mW. The resonator Q_{int} is 1.6 million and the f_{rep} is estimated to be around 433 GHz. **b**. Soliton microcomb spectrum from a $100\,\mu$m-radius AlN resonator (cross section: $1.0\times3.5\,\mu\mathrm{m}^2$) with a decreased f_{rep} of $\sim$220 GHz. The applied pump power is $\sim$1 W at a resonator Q_{int} of 3.0 million.

while μ indexes the relative azimuth mode number with respect to the pump ($\mu=0$).

Octave soliton microcombs. Our GVD engineered AlN resonators are coated with a SiO_2 protection layer, making it less susceptible to the ambient compared with the air-cladded Si_3N_4 counterpart [25–29]. An example of the resonator modal profile is shown in the inset of Fig. 2a. The top panel of Fig. 2a plots the D_{int} curve from a $50\,\mu$m-radius AlN resonator through numerical simulation (see Methods). In spite of the limited anomalous GVD window (light blue shade), octave microcomb operation is feasible via DW radiations at phase-matching conditions $D_{\mathrm{int}}=0$, allowing for spectral extension into normal GVD regimes (light orange shade). Note that the occurrence of such dual DWs benefits from the optimal film thickness in our AlN system, while the DW separation is agilely adjustable over one octave through the control of resonator's dimensions. (see Supplementary Section II). Around the telecom band, the D_{int} value (red dots) was characterized by calibrating the resonator's transmission with a fiber-based Mach–Zehnder interferometer [15, 17]. The experimental result matches well with the simulated one (inset of Fig. 2a) with an extracted $D_2/2\pi$ of $\sim$6.12 MHz.

We then explore soliton mode-locking based on a rapid frequency scan scheme to address the abrupt intracavity thermal variation associated with transitions into soliton states [15]. The soliton spectrum is recorded using two grating-based optical spectrum analyzers (OSAs, coverage of 350–1750 nm and 1500–3400 nm). The experimental setup is detailed in Supplementary Section II. The bottom panel of Fig. 2a plots the soliton spectrum from a $50\,\mu$m-radius AlN resonator, featuring a moderate f_{rep} of 433 GHz and an observable spectral span of 1.05–2.4 μm, exceeding one optical octave. Meanwhile, soliton-induced DW radiations occur at both ends of the spectrum, in agreement with the predicted D_{int} curves. Note that the low-frequency DW location matches well with the $D_{\mathrm{int}}=0$ position, while the high-frequency one exhibits an evident blue shift, which is ascribed to Raman-induced soliton red shifts relative to the pump frequency [45, 46]. This conclusion is supported by the soliton spectral simulation (red curve) when accounting for Raman effects (see Methods), while the intact low-frequency DW might

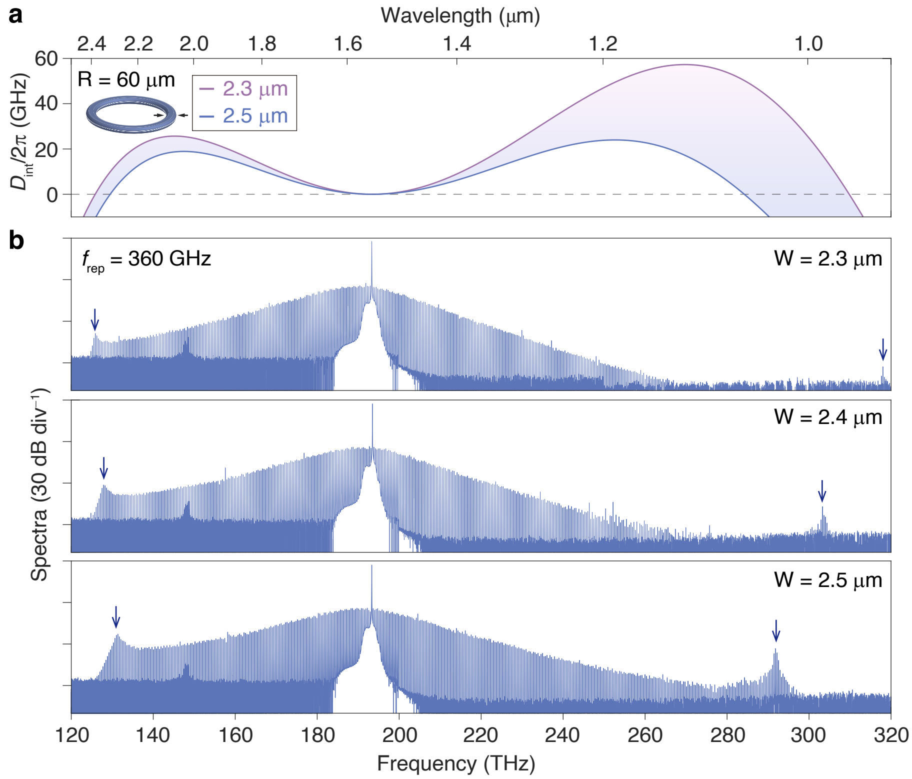

Fig. 3. **Octave soliton microcombs with agilely tunable spectra**. **a**. Engineered $D_{\rm int}$ curves of 60 μm-radius AlN resonators at varied widths of 2.3–2.5 μm revealed by the colored shadow regime. **b**. Corresponding soliton microcomb spectra at resonator widths of 2.3, 2.4, and 2.5 μm from the top to bottom panel, respectively. The $f_{\rm rep}$ is ∼360 GHz, while the vertical arrows in spectral wings indicate the emergence of DWs. Akin to Fig. 2a, high-frequency DWs here also exhibit an evident blue shift from the $D_{\rm int} = 0$ position. From a sech^2 fit, the corresponding temporal pulse duration is estimated to be ∼23, 22 and 19 fs (from top to bottom), respectively.

be a result of the cancellation of soliton recoils [11].

The single crystal nature of AlN thin films permits reproducible optical index in each manufacture run. This, in combination with their uniform film thickness control, leads to a high predictability for the dispersion engineering, making it feasible to predict octave soliton combs at various repetition rates. For instance, our GVD model indicates that octave spectra with repetition rates further decreased by two times are anticipated from 100 μm-radius AlN resonators at optimal widths of 3.3–3.5 μm (see Supplementary Section II). Figure 2b plots the recorded soliton comb spectrum at a resonator width of 3.5 μm, where a $f_{\rm rep}$ of ∼220 GHz and dual DWs separated by more than one octave are achieved simultaneously. Such a low $f_{\rm rep}$ is amenable for direct photodetection with state-of-the-art unitravelling-carrier photodiodes [47]. We also noticed the occurrence of a weak sharp spectrum around 130 THz, which might arise from modified local GVD due to avoided mode crossing[48]. In our nanophotonic platform, we could further predict resonator geometries for achieving octave solitons with an electronically detectable $f_{\rm rep}$ of ∼109 GHz (see Supplementary Section II). Nonetheless, the strong competition between Kerr nonlinearities and stimulated Raman scattering (SRS) must be taken into account since the free spectrum range (FSR) of the resonator is already smaller than the $A_1^{\rm TO}$ phonon linewidth (∼138 GHz) in AlN crystals [42].

Since the SHG from the auxiliary laser (1940–2000 nm) available in our laboratory is beyond the soliton spectral coverage shown in Fig. 2, we further adjust the resonator dimensions for extending microcomb spectra below 1 μm. As plotted in Fig. 3a, the phase-matching condition ($D_{\rm int} = 0$) for high-frequency DW radiations below 1 μm is fulfilled by elevating the resonator radius to 60 μm while maintaining its width around 2.3 μm. In the meantime, low-frequency DWs could also be expected and their spectral separation is adjustable by controlling the resonator width. Guided by the tailored $D_{\rm int}$ curves, we fabricated the AlN resonators and recorded octave soliton spectra at a $f_{\rm rep}$ of ∼360 GHz (Fig. 3b). Lithographic control of DW radiations (indicated by vertical arrows) is also verified by solely adjusting the resonator width, allowing the spectral extension below 1 μm (width of 2.3 or 2.4 μm). The low- and high-frequency DWs are found to exhibit distinct frequency shifting rates, consistent with the $D_{\rm int}$ prediction. The observable soliton spectra (from top to bottom of Fig. 3b) cover 1.5, 1.3, and

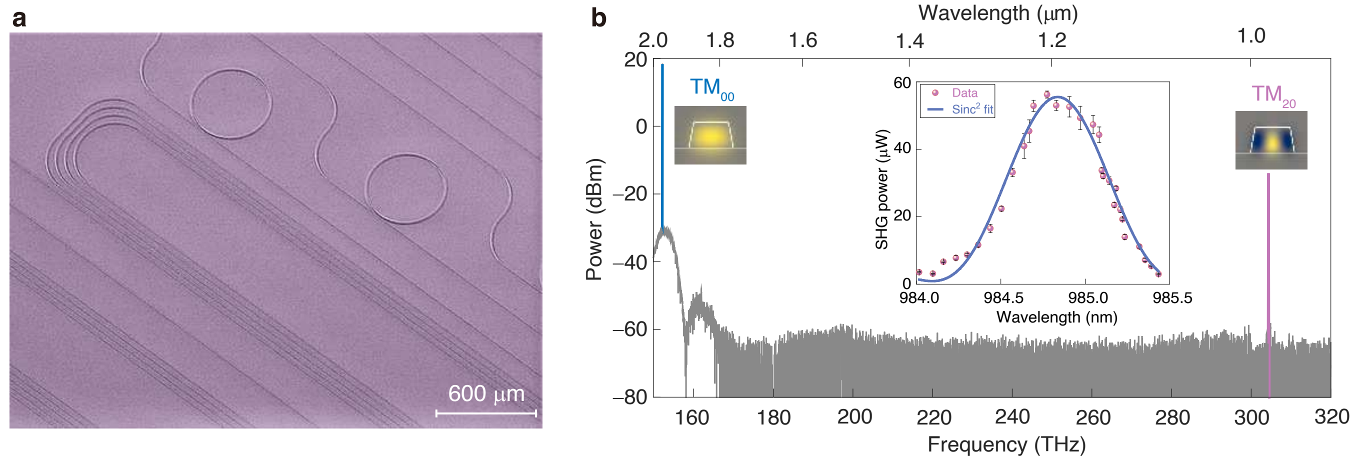

Fig. 4. **Second-harmonic generators.** **a**. Colored scanning electron microscope images of fabricated AlN nanophotonic chips composed of octave microcomb generators (microring resonators) and SHG waveguides (total length of 6 cm, not fully shown). **b**. SHG spectra collected from a modal phase-matched waveguide (width of 1.395 μm) at an on-chip $1f$ power of 355 mW. Insets: modal profiles of the pump (TM_{00}) and SHG (TM_{20}) waves as well as the wavelength-dependent SHG power (pink dots), where a sinc^2-function fit (blue curve) is applied. The error bars reflect the SHG power variation from continuous three measurements.

1.2 optical octaves by normalizing the total span (Δf) to its beginning frequency (f_1), that is $\Delta f/f_1$. Such a definition permits a fair comparison among soliton microcomb generation in distinct pump regimes across different material platforms, suggesting high competitiveness of our AlN microcomb span comparing to state-of-the-art values reported in Si_3N_4 microresonators [26].

On-chip second harmonic generator. We then explore the co-integration of SHG based on the χ^2 susceptibility of AlN for matching the DW peak below 1 μm (middle panel of Fig. 3b). To fulfill the demanding requirement of spectral overlaps with the microcomb, we adopt a straight waveguide configuration, which allows a broader phase-matching condition albeit at the cost of reduced conversion efficiencies comparing to its counterpart using dual-resonant microresonators [34, 49]. Through modeling, we predict an optimal waveguide width of $\sim$1.38 μm for fulfilling the modal-phase-matching condition (see Supplementary Section III), while the actual waveguide width was lithographically stepped from 1.32 to 1.46 μm (spacing of 5 nm) accounting for possible deviations during the manufacturing process.

Figure 4a shows a section of 6 cm-long SHG waveguides co-fabricated with the microcomb generator. At a fixed fundamental wavelength (1970 nm), we located the phase-matching waveguide at the width of 1.395 μm, close to the predicted width. The corresponding SHG spectra are plotted in Fig. 4b, where we achieve a high off-chip SHG power over 50 μW by boosting the fundamental pump power from a thulium-doped fiber amplifier to compensate the SHG efficiency (see Supplementary Section III). In the meantime, the wavelength-dependent SHG power shown in the inset indicates a large 3-dB phase-matching bandwidth of $\sim$0.8 nm, which, together with an external heater for thermal fine-tuning, is sufficient to cover the target comb lines for subsequent heterodyne beating.

Nanophotonic f–$2f$ interferometry. By combining outgoing light from optimal AlN soliton and SHG generators on the calibrated OSAs, we are able to estimate the f–$2f$ beatnote frequency to be approximately 32 GHz limited by the resolution of the OSAs. To electronically access the f_{ceo} signal in real time, we employ a scheme sketched in Fig. 5a. The recorded soliton spectrum after suppressing pump light by a fiber Bragg grating (FBG) indicates a high off-chip power close to -40 dBm for the high-frequency DW (see Supplementary Section III). Meanwhile, a wavelength-division multiplexer (WMD) is utilized to separate the f and $2f$ frequency components before sent into the photodetectors (PDs). Two tunable radio frequency (RF) synthesizers are introduced as the local oscillators (LO1 and LO2) to down convert the photodetector signals for effective capture of f–$2f$ beat signal at a convenient low-frequency band with an electronic spectrum analyzer (ESA, range of 20 Hz–26.5 GHz).

As highlighted in Fig. 5b, we record two down-converted beatnotes of Δf_1 and Δf_2 with a signal-to-noise ratio of 10 dB at a resolution bandwidth of 1 MHz. Much higher signal-to-noise ratios are anticipated by applying a finer detection bandwidth upon locking the telecom pump laser as well as the f_{ceo} frequency [23, 24]. The corresponding f–$2f$ beatnote is $\overline{f_{\mathrm{ceo}}} = 2f_{\mathrm{LO1}} + f_{\mathrm{LO2}} - \Delta f_2$ (inset of Fig. 5b) since the local oscillator frequencies f_{LO1} and f_{LO2} are chosen to be larger than beatnotes of δ_1 and δ_2. We also note that the actual f_{ceo} in the current device equals to $\mathrm{FSR} - \overline{f_{\mathrm{ceo}}}$, which is unveiled by tuning the relative positions of auxiliary laser and comb teeth frequencies, indicating the involvement of f_{n} and $f_{\mathrm{2n+1}}$ comb lines in the heterodyne beating (see Supplementary Section III). On the other

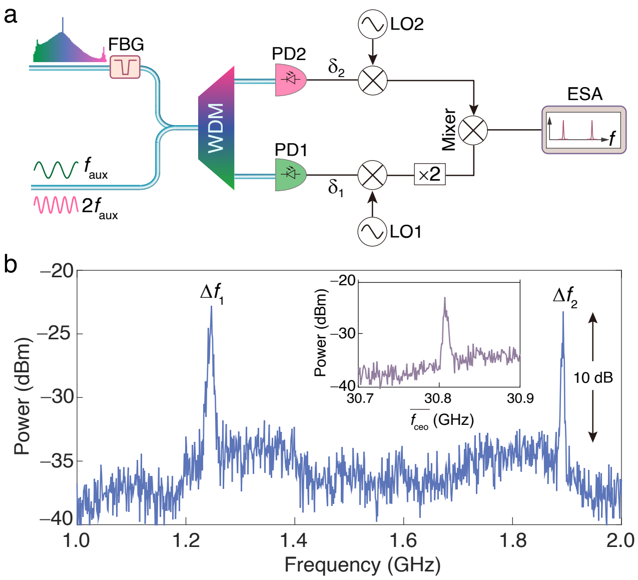

Fig. 5. f–$2f$ **heterodyne measurement.** **a**. Schematic diagram for assessing the f_{ceo}. The symbol "×2" indicates a RF frequency doubler. The experimental details are introduced in Supplementary Section III. **b**. Free-running f–$2f$ beatnotes after the down-conversion process, suggesting a signal-to-noise ratio of 10 dB at a resolution bandwidth of 1 MHz. The local oscillator frequencies f_{LO1} and f_{LO2} are chosen to be 11.8 and 9.1 GHz, respectively. Inset: the equivalent curve of $\overline{f_{\text{ceo}}} = 2f_{\text{LO1}} + f_{\text{LO2}} - \Delta f_2$.

hand, the f_{LO1} and f_{LO2} frequencies are freely adjustable up to 40 and 20 GHz in our scheme, which could further expand the accessible range of f_{ceo} frequency based on the down-conversion process presented here. Meanwhile, the RF synthesizers are synchronized to a common external frequency reference, suggesting that the captured down-converted f–$2f$ signals are available for further locking the comb teeth in a feedback loop as reported in Ref. [28].

III. DISCUSSION

We demonstrate nanophotonic implementation of f–$2f$ interferometry by leveraging $\chi^{(3)}$ octave solitons and $\chi^{(2)}$ SHG co-fabricated from a non-centrosymmetric AlN photonic platform. Thanks to agile GVD engineering offered by epitaxial AlN thin films, our octave soliton microcombs can reliably produce dual DWs and sub-THz repetition rates (220–433 GHz) that are accessible with unitravelling-carrier photodiodes. The overall soliton spectral span is adjustable up to 1.5 octave, on a par with state-of-the-art values (1.4 octave) reported in Si_3N_4 microresonators. We further perform the f_{ceo} measurement with the aid of an auxiliary laser for enabling SHG in phase-matched AlN waveguides, thus allowing for spectral overlap with the desired octave soliton.

For future development, the spectral restriction of octave solitons for matching with the auxiliary laser wavelength can be relaxed by exploiting high-efficiency SHG in dual-resonant microresonators, which allows direct doubling of a selected comb line in the low frequency DW band [50]. Meanwhile, the octave comb's repetition rate can be further reduced by leveraging on-chip Pockels electro-optical frequency division [51]. By shifting the phase matching condition for SHG, it is also possible to extend octave solitons into the near-visible band, giving access to self-locked near-visible microcombs for precision metrology. Besides, the exploration of other non-centrosymmetric photonic media such as LN, GaAs and gallium phosphide could be envisioned [37, 46, 52]. For instance, by exploiting periodically poled LN thin films [53], it is likely to simultaneously achieve phase matched $\chi^{(2)}$ and octave $\chi^{(3)}$ interactions in a single microring resonator, thus simplifying the photonic architectures. Our results represent an important milestone to unlock the potentials of octave microcomb technologies for portable applications.

IV. METHODS

Nanofabrication. The surface roughness and crystal quality of our AlN thin films were respectively characterized by an atomic force microscope and an X-ray diffraction scan, indicating a root-mean-square roughness of 0.2 nm in $1 \times 1\,\mu\text{m}^2$ region and an FWHM linewidth of ∼46 and 1000 arcsec along (002) and (102) crystal orientations, respectively. The film thickness was mapped by a spectroscopic ellipsometer (J.A. Woollam M-2000), providing a quick and preliminary selection of the desired AlN piece for octave soliton generation with dual DWs. As shown in Supplementary Section I, in spite of varied film thicknesses across a 2-inch AlN wafer, we can reliably locate the desired region for reproducible octave device fabrication.

To further reduce the propagation loss, the AlN photonic chips were annealed at 1000 °C for 2 hours. The resonator Q-factors were probed by sweeping a tunable laser (Santec TSL-710) across the cavity resonances and then fitted by a Lorentzian function. In the 100 μm-radius AlN resonators (width of 3.5 μm), we achieve a recorded Q_{int} of 3.0 million, while the 50 μm-radius resonators (width of 2.3 μm) exhibit a decreased Q_{int} of 1.6 million, indicating the dominant sidewall scattering loss of our current fabrication technology. The related resonance curves are plotted in Supplementary Section I.

Numerical simulation. The D_{int} of the AlN resonators is investigated using a finite element method (FEM) by simultaneously accounting for the material and geometric chromatic dispersion. The overall D_{int} value is approximated with a fifth-order polynomial fit applied to the simulated modal angular frequencies: $\omega_\mu = \omega_0 + \mu D_1 + D_{\text{int}}$, where $D_1/(2\pi)$ is the resonator's FSR at the pump mode $\mu = 0$.

The spectral dynamics of octave soliton microcombs is numerically explored based on nonlinear coupled mode equations by incorporating the Raman effect [46, 54]:

$$\frac{\partial}{\partial t}a_\mu = -(\frac{\kappa_\mu}{2}+i\Delta^a_\mu)a_\mu + ig_{\mathrm{K}}\sum_{k,l,n} a^*_k a_l a_n \delta(l+n-k-\mu) - ig_{\mathrm{R}}\sum_{k,l} a_l\big[\mathcal{R}_k\delta(l+k-\mu)+\mathcal{R}^*_k\delta(l-k-\mu)\big]+\xi_{\mathrm{P}} \quad (3)$$

$$\frac{\partial}{\partial t}\mathcal{R}_\mu = -(\frac{\gamma_{\mathrm{R}}}{2}+i\Delta^{\mathrm{R}}_\mu)\mathcal{R}_\mu - ig_{\mathrm{R}}\sum_{k,l} a^*_k a_l \delta(l-k-\mu) \quad (4)$$

Here a and $\mathcal{R}$ are the mode amplitudes of cavity photons and Raman phonons with subscripts k, l, n being the mode indices, while g_{K} and g_{R} represent the nonlinear coupling strength of Kerr and Raman processes, respectively. The driving signal strength is $\xi_{\mathrm{P}} = \delta(\mu)\sqrt{\frac{\kappa_{\mathrm{e},0}P_{\mathrm{in}}}{\hbar\omega_{\mathrm{p}}}}$ at an on-chip pump power P_{in}, κ_μ ($\kappa_{\mathrm{e},\mu}$) denotes the total (external) cavity decay rate of the μ^{th} photon mode, and γ_{R} is the Raman phonon decay rate. The detuning from a D_1-spaced frequency grid is indicated by $\Delta^a_\mu = \omega_\mu - \omega_{\mathrm{P}} - \mu D_1$ and $\Delta^{\mathrm{R}}_\mu = \omega_{\mathrm{R}} - \mu D_1$ with ω_{P} and ω_{R} being pump and Raman shift angular frequencies, respectively.

In the simulation, we set the time derivative of Raman items in Eq. 4 to zero to speed up the computation since the decay rate of phonons is much larger than that of photons. We also consider frequency-independent $\kappa_\mu/(2\pi) \approx 120$ MHz and $\kappa_{\mathrm{e},\mu}/(2\pi) \approx 75$ MHz based on measured Q-factors of 50 μm-radius AlN resonators in Fig. 2a. Because incident light is TM-polarized, the involved $\mathrm{A}_1^{\mathrm{TO}}$ Raman phonon in AlN exhibits an $\omega_{\mathrm{R}}/(2\pi) \approx 18.3$ THz with an FWHM of $\gamma_{\mathrm{R}}/(2\pi) \approx 138$ GHz [41]. The $g_{\mathrm{K}}/2\pi$ is calculated to be 0.73 Hz for a given nonlinear refractive index $n_2 = 2.3\times10^{-19}$ m^2/W, while an optimal $g_{\mathrm{R}}/2\pi = 0.29$ MHz is adopted, resulting in a soliton spectrum matching well with the measured one in Fig. 2a. The simulated high frequency DW also exhibits an evident blue shift comparing with the case of $g_{\mathrm{R}}/2\pi = 0$ MHz (see Supplementary Section II).

V. DATA AVAILABILITY

The data that support the findings of this study are available from the corresponding authors upon reasonable request.

VI. REFERENCES

[1] T. Fortier and E. Baumann, "20 years of developments in optical frequency comb technology and applications," Commun. Phys. **2**, 153 (2019).

[2] D. Waldburger, A. S. Mayer, C. G. E. Alfieri, J. Nürnberg, A. R. Johnson, X. Ji, A. Klenner, Y. Okawachi, M. Lipson, A. L. Gaeta, and U. Keller, "Tightly locked optical frequency comb from a semiconductor disk laser," Opt. Express **27**, 1786 (2019).

[3] M. Zhang, B. Buscaino, C. Wang, A. Shams-Ansari, C. Reimer, R. Zhu, J. M. Kahn, and M. Lončar, "Broadband electro-optic frequency comb generation in a lithium niobate microring resonator," Nature **568**, 373 (2019).

[4] A. L. Gaeta, M. Lipson, and T. J. Kippenberg, "Photonic-chip-based frequency combs," Nat. Photon. **13**, 158 (2019).

[5] A. Pasquazi, M. Peccianti, L. Razzari, D. J. Moss, S. Coen, M. Erkintalo, Y. K. Chembo, T. Hansson, S. Wabnitz, P. Del'Haye, X. Xue, A. M. Weiner, and R. Morandotti, "Micro-combs: A novel generation of optical sources," Phys. Rep. **729**, 1 (2018).

[6] T. J. Kippenberg, A. L. Gaeta, M. Lipson, and M. L. Gorodetsky, "Dissipative kerr solitons in optical microresonators," Science **361**, eaan8083 (2018).

[7] B. Stern, X. Ji, Y. Okawachi, A. L. Gaeta, and M. Lipson, "Battery-operated integrated frequency comb generator," Nature **562**, 401 (2018).

[8] A. S. Raja, A. S. Voloshin, H. Guo, S. E. Agafonova, J. Liu, A. S. Gorodnitskiy, M. Karpov, N. G. Pavlov, E. Lucas, R. R. Galiev, A. E. Shitikov, J. D. Jost, M. L. Gorodetsky, and T. J. Kippenberg, "Electrically pumped photonic integrated soliton microcomb," Nat. Commun. **10**, 680 (2019).

[9] T. Herr, V. Brasch, J. D. Jost, C. Y. Wang, N. M. Kondratiev, M. L. Gorodetsky, and T. J. Kippenberg, "Temporal solitons in optical microresonators," Nat. Photon. **8**, 145 (2014).

[10] X. Xue, Y. Xuan, Y. Liu, P.-H. Wang, S. Chen, J. Wang, D. E. Leaird, M. Qi, and A. M. Weiner, "Mode-locked dark pulse kerr combs in normal-dispersion microresonators," Nat. Photon. **9**, 594 (2015).

[11] V. Brasch, M. Geiselmann, T. Herr, G. Lihachev, M. H. P. Pfeiffer, M. L. Gorodetsky, and T. J. Kippenberg, "Photonic chip-based optical frequency comb using soliton cherenkov radiation," Science **351**, 357 (2015).

[12] X. Yi, Q.-F. Yang, K. Y. Yang, M.-G. Suh, and K. Vahala, "Soliton frequency comb at microwave rates in a high-q silica microresonator," Optica **2**, 1078 (2015).

[13] C. Joshi, J. K. Jang, K. Luke, X. Ji, S. A. Miller, A. Klenner, Y. Okawachi, M. Lipson, and A. L. Gaeta, "Thermally controlled comb generation and soliton modelocking in microresonators," Opt. Lett. **41**, 2565 (2016).

[14] M. Yu, Y. Okawachi, A. G. Griffith, M. Lipson, and A. L. Gaeta, "Mode-locked mid-infrared frequency combs in a silicon microresonator," Optica **3**, 854 (2016).

[15] Z. Gong, A. Bruch, M. Shen, X. Guo, H. Jung, L. Fan, X. Liu, L. Zhang, J. Wang, J. Li, J. Yan, and H. X. Tang, "High-fidelity cavity soliton generation in crystalline AlN micro-ring resonators," Opt. Lett. **43**, 4366 (2018).

[16] Y. He, Q.-F. Yang, J. Ling, R. Luo, H. Liang, M. Li, B. Shen, H. Wang, K. Vahala, and Q. Lin, "Self-starting bi-chromatic linbo3 soliton microcomb," Optica **6**, 1138 (2019).

[17] Z. Gong, X. Liu, Y. Xu, M. Xu, J. B. Surya, J. Lu, A. Bruch, C. Zou, and H. X. Tang, "Soliton microcomb generation at 2 μm in z-cut lithium niobate microring resonators," Opt. Lett. **44**, 3182 (2019).

[18] Q.-F. Yang, X. Yi, K. Y. Yang, and K. Vahala, "Stokes solitons in optical microcavities," Nat. Phys. **13**, 53 (2016).

[19] H. Guo, M. Karpov, E. Lucas, A. Kordts, M. H. P. Pfeiffer, V. Brasch, G. Lihachev, V. E. Lobanov, M. L. Gorodetsky, and T. J. Kippenberg, "Universal dynamics and deterministic switching of dissipative kerr solitons in optical microresonators," Nat. Phys. **13**, 94 (2016).

[20] D. C. Cole, E. S. Lamb, P. Del'Haye, S. A. Diddams, and S. B. Papp, "Soliton crystals in kerr resonators," Nat. Photon. **11**, 671 (2017).

[21] D. J. Jones, "Carrier-envelope phase control of femtosecond mode-locked lasers and direct optical frequency synthesis," Science **288**, 635 (2000).

[22] M. Giunta, R. Holzwarth, M. Fischer, W. Hansel, T. Steinmetz, M. Lessing, S. Holzberger, C. Cleff, T. W. Hansch, and M. Mei, "20 years and 20 decimal digits: A journey with optical frequency combs," IEEE Photon. Technol. Lett. **31**, 1898 (2019).

[23] D. T. Spencer, T. Drake, T. C. Briles, J. Stone, L. C. Sinclair, C. Fredrick, Q. Li, D. Westly, B. R. Ilic, A. Bluestone, N. Volet, T. Komljenovic, L. Chang, S. H. Lee, D. Y. Oh, M.-G. Suh, K. Y. Yang, M. H. P. Pfeiffer, T. J. Kippenberg, E. Norberg, L. Theogarajan, K. Vahala, N. R. Newbury, K. Srinivasan, J. E. Bowers, S. A. Diddams, and S. B. Papp, "An optical-frequency synthesizer using integrated photonics," Nature **557**, 81 (2018).

[24] Z. L. Newman, V. Maurice, T. Drake, J. R. Stone, T. C. Briles, D. T. Spencer, C. Fredrick, Q. Li, D. Westly, B. R. Ilic, B. Shen, M.-G. Suh, K. Y. Yang, C. Johnson, D. M. S. Johnson, L. Hollberg, K. J. Vahala, K. Srinivasan, S. A. Diddams, J. Kitching, S. B. Papp, and M. T. Hummon, "Architecture for the photonic integration of an optical atomic clock," Optica **6**, 680 (2019).

[25] Q. Li, T. C. Briles, D. A. Westly, T. E. Drake, J. R. Stone, B. R. Ilic, S. A. Diddams, S. B. Papp, and K. Srinivasan, "Stably accessing octave-spanning microresonator frequency combs in the soliton regime," Optica **4**, 193 (2017).

[26] M. H. P. Pfeiffer, C. Herkommer, J. Liu, H. Guo, M. Karpov, E. Lucas, M. Zervas, and T. J. Kippenberg, "Octave-spanning dissipative kerr soliton frequency combs in si_3n_4 microresonators," Optica **4**, 684 (2017).

[27] S.-P. Yu, T. C. Briles, G. T. Moille, X. Lu, S. A. Diddams, K. Srinivasan, and S. B. Papp, "Tuning kerr-soliton frequency combs to atomic resonances," Phys. Rev. Appl. **11**, 044017 (2019).

[28] T. E. Drake, T. C. Briles, J. R. Stone, D. T. Spencer, D. R. Carlson, D. D. Hickstein, Q. Li, D. Westly, K. Srinivasan, S. A. Diddams, and S. B. Papp, "Terahertz-rate kerr-microresonator optical clockwork," Phys. Rev. X **9**, 031023 (2019).

[29] T. C. Briles, J. R. Stone, T. E. Drake, D. T. Spencer, C. Fredrick, Q. Li, D. Westly, B. R. Ilic, K. Srinivasan, S. A. Diddams, and S. B. Papp, "Interlocking kerr-microresonator frequency combs for microwave to optical synthesis," Opt. Lett. **43**, 2933 (2018).

[30] C. Xiong, W. H. Pernice, X. Sun, C. Schuck, K. Y. Fong, and H. X. Tang, "Aluminum nitride as a new material for chip-scale optomechanics and nonlinear optics," New J. Phys. **14**, 095014 (2012).

[31] M. Kneissl, T.-Y. Seong, J. Han, and H. Amano, "The emergence and prospects of deep-ultraviolet light-emitting diode technologies," Nat. Photon. **13**, 233 (2019).

[32] S. G. Bishop, J. P. Hadden, F. Alzahrani, R. Hekmati, D. L. Huffaker, W. W. Langbein, and A. J. Bennett, "Room temperature quantum emitter in aluminum nitride," ACS Photonics **7**, 1636 (2020).

[33] T.-J. Lu, B. Lienhard, K.-Y. Jeong, H. Moon, A. Iranmanesh, G. Grosso, and D. R. Englund, "Bright high-purity quantum emitters in aluminum nitride integrated photonics," ACS Photonics **7**, 2650– (2020).

[34] A. W. Bruch, X. Liu, X. Guo, J. B. Surya, Z. Gong, L. Zhang, J. Wang, J. Yan, and H. X. Tang, "17000%/w second-harmonic conversion efficiency in single-crystalline aluminum nitride microresonators," Appl. Phys. Lett. **113**, 131102 (2018).

[35] X. Liu, A. W. Bruch, J. Lu, Z. Gong, J. B. Surya, L. Zhang, J. Wang, J. Yan, and H. X. Tang, "Beyond 100 THz-spanning ultraviolet frequency combs in a non-centrosymmetric crystalline waveguide," Nat. Commun. **10**, 2971 (2019).

[36] A. W. Bruch, X. Liu, Z. Gong, J. B. Surya, M. Li, C.-L. Zou, and H. X. Tang, "Pockels soliton microcomb," Nat. Photon. (2020), 10.1038/s41566-020-00704-8.

[37] L. Chang, A. Boes, X. Guo, D. T. Spencer, M. J. Kennedy, J. D. Peters, N. Volet, J. Chiles, A. Kowligy, N. Nader, D. D. Hickstein, E. J. Stanton, S. A. Diddams, S. B. Papp, and J. E. Bowers, "Heterogeneously integrated gaas waveguides on insulator for efficient frequency conversion," Laser & Photon. Rev. **12**, 1800149 (2018).

[38] D. D. Hickstein, H. Jung, D. R. Carlson, A. Lind, I. Coddington, K. Srinivasan, G. G. Ycas, D. C. Cole, A. Kowligy, C. Fredrick, S. Droste, E. S. Lamb, N. R. Newbury, H. X. Tang, S. A. Diddams, and S. B. Papp, "Ultrabroadband supercontinuum generation and frequency-comb stabilization using on-chip waveguides with both cubic and quadratic nonlinearities," Phys. Rev. Appl. **8**, 014025 (2017).

[39] M. Yu, B. Desiatov, Y. Okawachi, A. L. Gaeta, and M. Lončar, "Coherent two-octave-spanning supercontinuum generation in lithium-niobate waveguides," Opt. Lett. **44**, 1222 (2019).

[40] Y. Okawachi, M. Yu, B. Desiatov, B. Y. Kim, T. Hansson, M. Lončar, and A. L. Gaeta, "Chip-based self-referencing using integrated lithium niobate waveguides," Optica **7**, 702 (2020).

[41] X. Liu, C. Sun, B. Xiong, L. Wang, J. Wang, Y. Han, Z. Hao, H. Li, Y. Luo, J. Yan, *et al.*, "Integrated continuous-wave aluminum nitride raman laser," Optica **4**, 893 (2017).

[42] X. Liu, C. Sun, B. Xiong, L. Wang, J. Wang, Y. Han, Z. Hao, H. Li, Y. Luo, J. Yan, *et al.*, "Integrated high-q crystalline aln microresonators for broadband kerr and raman frequency combs," ACS Photonics **5**, 1943 (2018).

[43] X. Liu, A. W. Bruch, Z. Gong, J. Lu, J. B. Surya, L. Zhang, J. Wang, J. Yan, and H. X. Tang, "Ultra-high-q uv microring resonators based on a single-crystalline aln platform," Optica **5**, 1279 (2018).

[44] A. Majkić, A. Franke, R. Kirste, R. Schlesser, R. Collazo, Z. Sitar, and M. Zgonik, "Optical nonlinear and electro-optical coefficients in bulk aluminium nitride single crystals," Phys. Status Solidi B **254**, 1700077 (2017).

[45] M. Karpov, H. Guo, A. Kordts, V. Brasch, M. H. Pfeiffer, M. Zervas, M. Geiselmann, and T. J. Kippenberg, "Raman self-frequency shift of dissipative kerr solitons in

an optical microresonator," Phys. Rev. Lett. **116**, 103902 (2016).

[46] Z. Gong, X. Liu, Y. Xu, and H. X. Tang, "Near-octave lithium niobate soliton microcomb," Optica **7**, 1275 (2020).

[47] S. Zhang, J. M. Silver, X. Shang, L. Del Bino, N. M. Ridler, and P. Del'Haye, "Terahertz wave generation using a soliton microcomb," Opt. Express **27**, 35257 (2019).

[48] X. Yi, Q.-F. Yang, X. Zhang, K. Y. Yang, X. Li, and K. Vahala, "Single-mode dispersive waves and soliton microcomb dynamics," Nat. Commun. **8**, 14869 (2017).

[49] A. W. Bruch, X. Liu, J. B. Surya, C.-L. Zou, and H. X. Tang, "On-chip $\chi(2)$ microring optical parametric oscillator," Optica **6**, 1361 (2019).

[50] J. B. Surya, X. Guo, C.-L. Zou, and H. X. Tang, "Control of second-harmonic generation in doubly resonant aluminum nitride microrings to address a rubidium two-photon clock transition," Opt. Lett. **43**, 2696 (2018).

[51] J. Li, X. Yi, H. Lee, S. A. Diddams, and K. J. Vahala, "Electro-optical frequency division and stable microwave synthesis," Science **345**, 309 (2014).

[52] D. J. Wilson, K. Schneider, S. Hönl, M. Anderson, Y. Baumgartner, L. Czornomaz, T. J. Kippenberg, and P. Seidler, "Integrated gallium phosphide nonlinear photonics," Nat. Photon. **14**, 57 (2019).

[53] J. Lu, J. B. Surya, X. Liu, A. W. Bruch, Z. Gong, Y. Xu, and H. X. Tang, "Periodically poled thin-film lithium niobate microring resonators with a second-harmonic generation efficiency of 250,000%/w," Optica **6**, 1455 (2019).

[54] Z. Gong, M. Li, X. Liu, Y. Xu, J. Lu, A. Bruch, J. B. Surya, C. Zou, and H. X. Tang, "Photonic dissipation control for kerr soliton generation in strongly raman-active media," Phys. Rev. Lett. **125**, 183901 (2020).

Acknowledgements. This work was supported by DARPA SCOUT (W31P4Q-15-1-0006). H.X.T. acknowledges partial support from DARPA's ACES program as part of the Draper-NIST collaboration (HR0011-16-C-0118) and DARPA's A-Phi program with a subcontract from Sandia labs (DENA0003525). The authors thank Y. Sun, S. Rinehart and K. Woods in Yale cleanrooms and M. Rooks in YINQE for assistance in the device fabrication, and J. Xie and M. Xu in the laboratory for the microwave circuit discussion.

Author contributions. H.X.T and X.L conceived the idea. X.L. performed the device design, fabrication and measurement with the assistance from Z.G., A.B., J.S. and J.L.. Z.G. and X.L. performed the soliton simulation. X.L. and H.X.T. wrote the manuscript with the input from all other authors. H.X.T supervised the project.

Competing interests. The authors declare no competing interests.

Additional information. Supplementary information accompanies this manuscript.

Figures

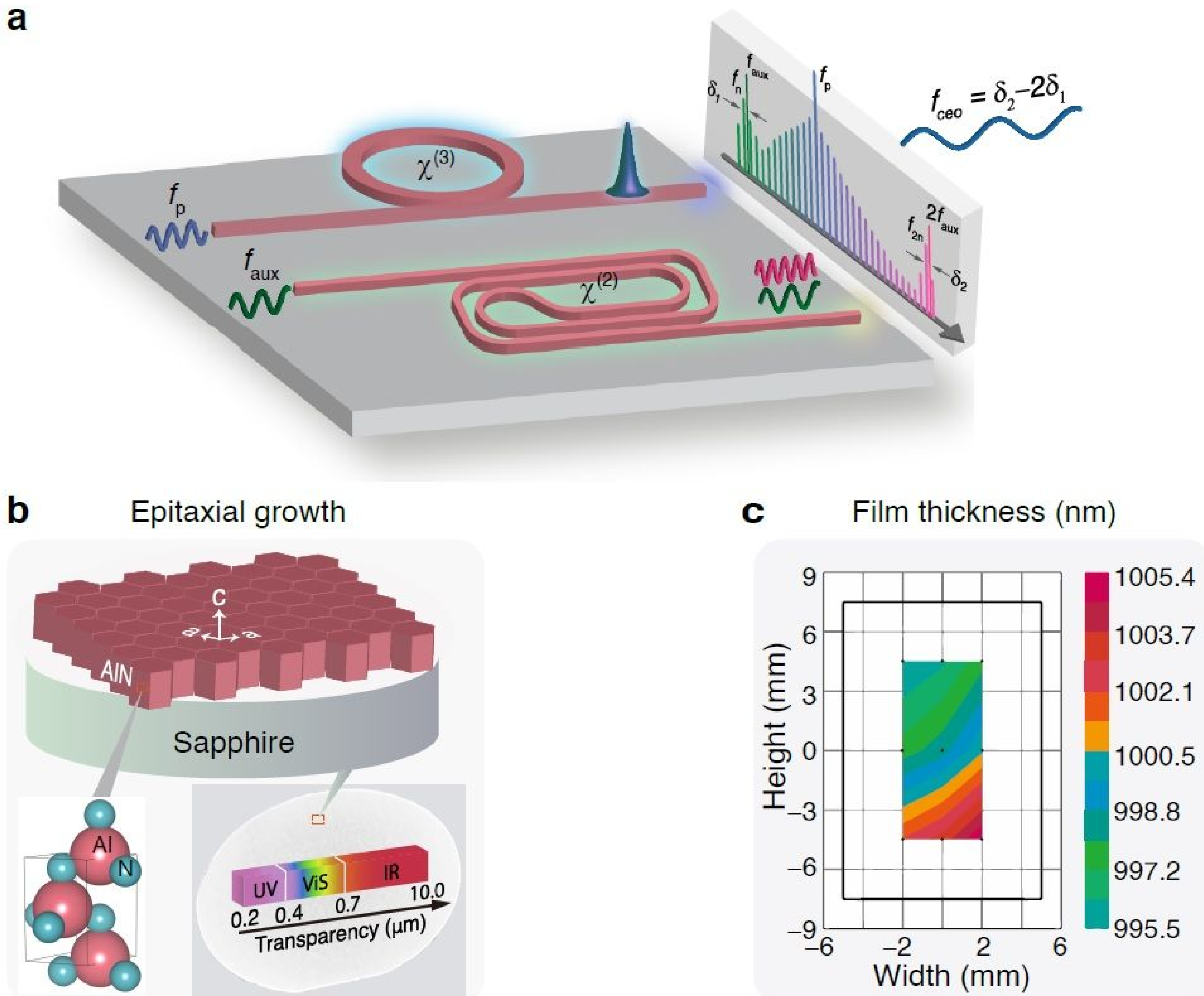

Figure 1

Experimental scheme. (see Manuscript file for full figure caption)

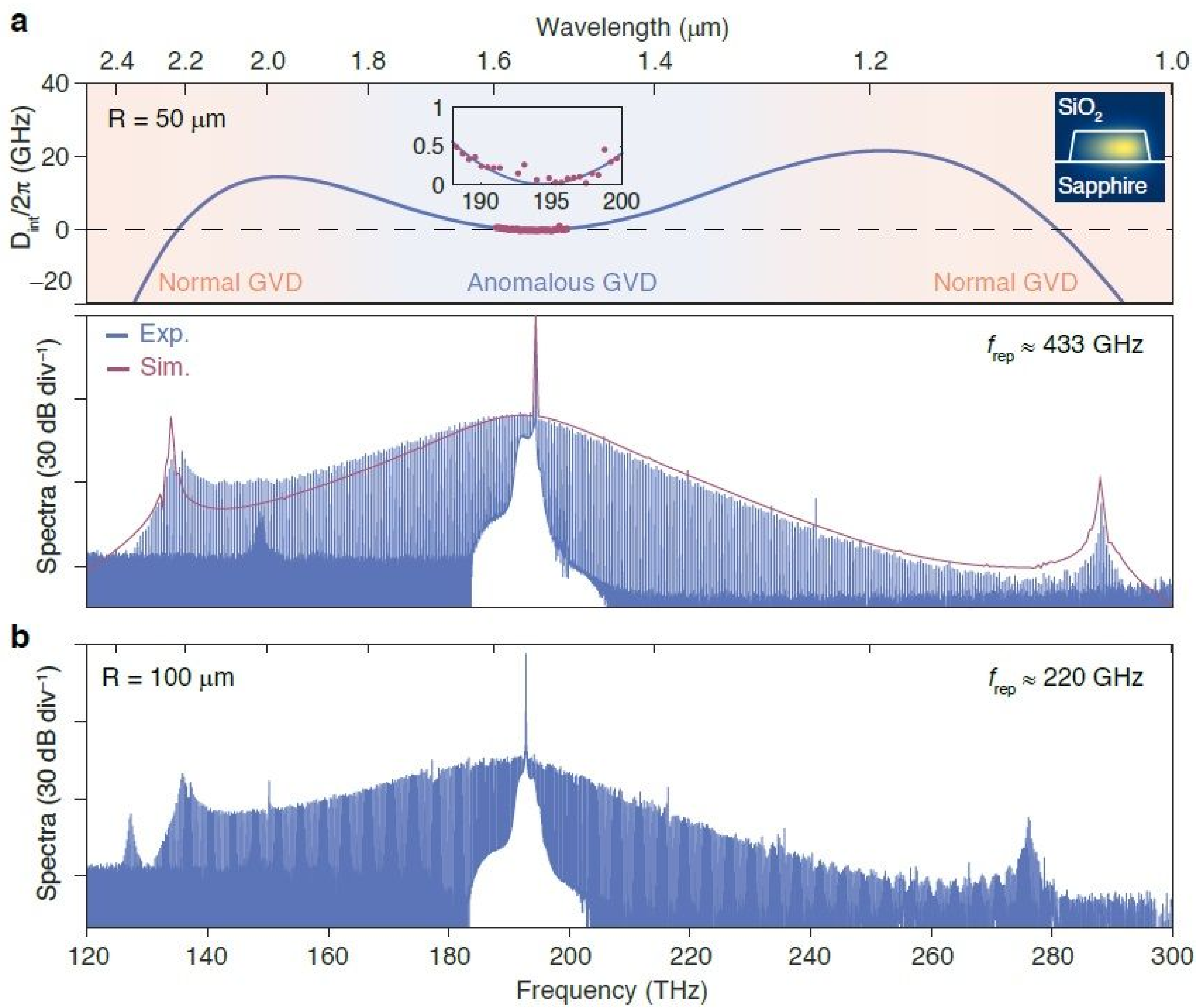

Figure 2

Octave soliton microcombs at hundreds of gigahertz repetition rates. (see Manuscript file for full figure caption)

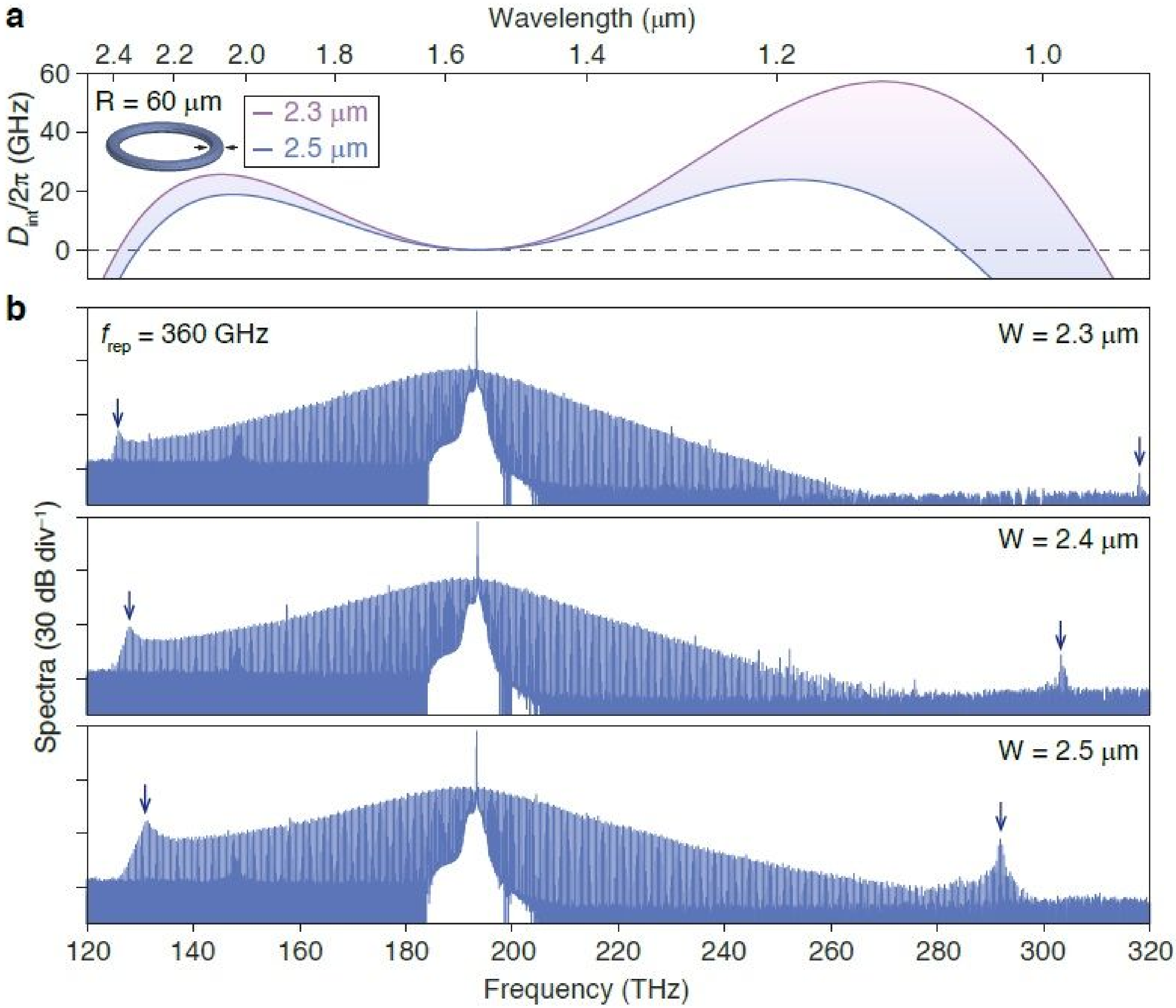

Figure 3

Octave soliton microcombs with agilely tunable spectra. (see Manuscript file for full figure caption)

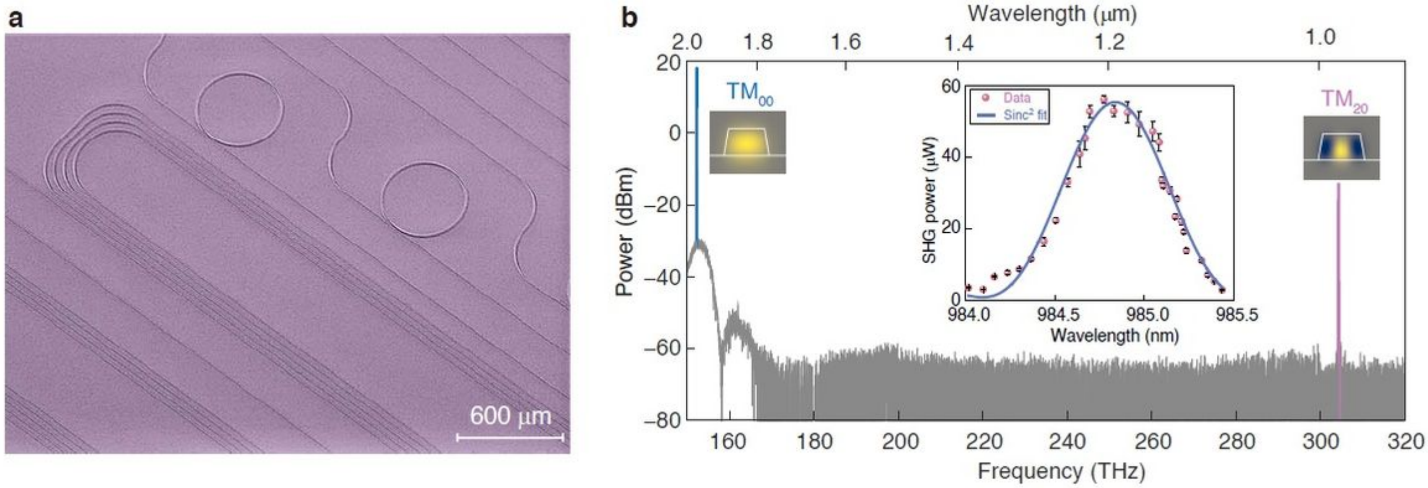

Figure 4

Second-harmonic generators. (see Manuscript file for full figure caption)

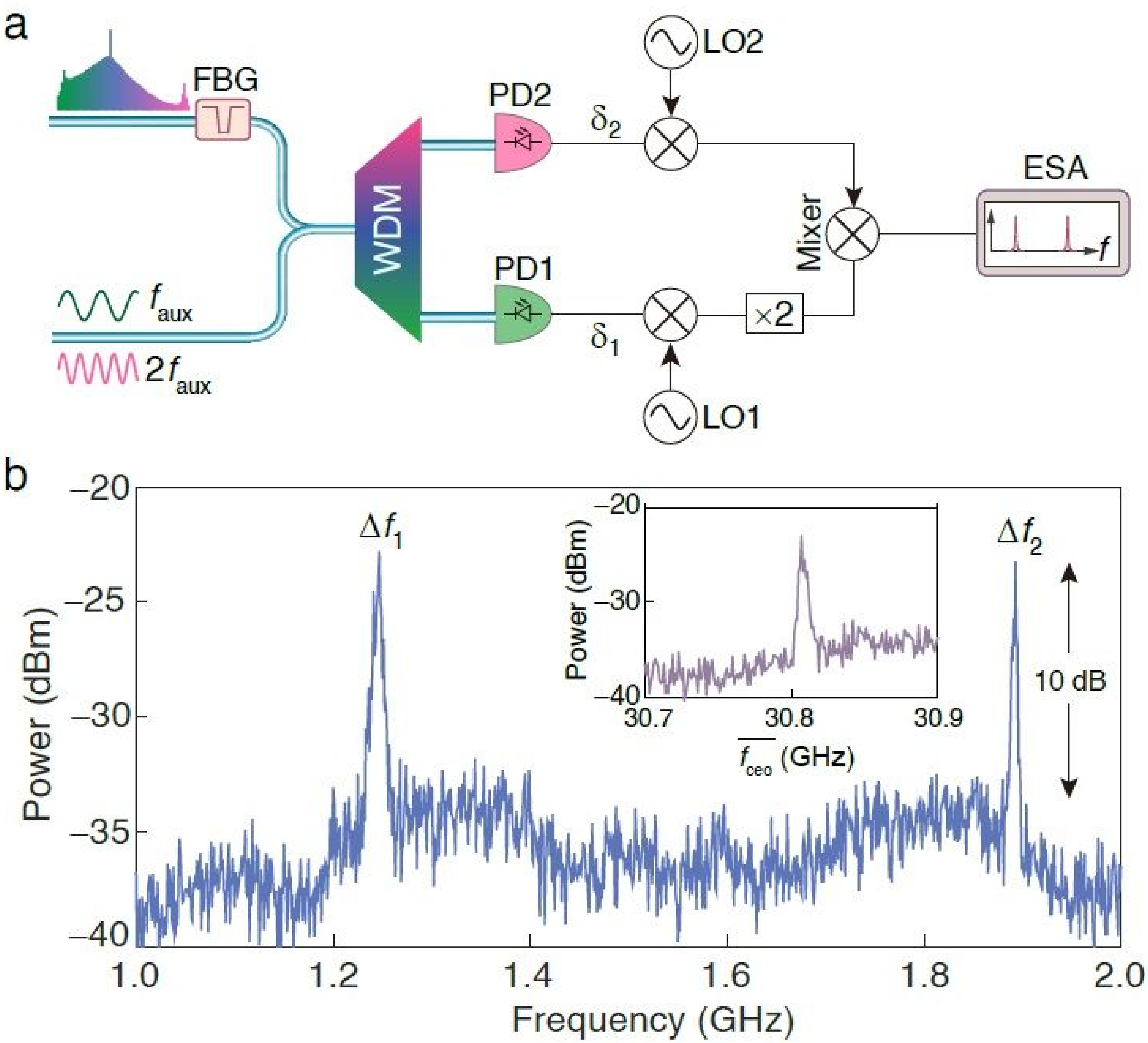

Figure 5

f-2f heterodyne measurement. (see Manuscript file for full figure caption)

Supplementary Files

This is a list of supplementary files associated with this preprint. Click to download.

- Supplementary.pdf